Blood Flow Dynamics in Saccular Aneurysm Models of the Basilar Artery

Alvaro A. Valencia
Mechanical Engineering,
Universidad de Chile,
Casilla 2777, Santiago, Chile
e-mail: alvalenc@ing.uchile.cl

Amador M. Guzmán
Mechanical Engineering,
Universidad de Santiago de Chile,
Casilla 10233, Santiago, Chile
e-mail: aguzman@usach.cl

Ender A. Finol
ASME Member
Institute for Complex Engineered Systems,
Biomedical Engineering,
Carnegie Mellon University,
Pittsburgh, PA 15213-3890
e-mail: finole@cmu.edu

Cristina H. Amon
Raymond J. Lane Distinguished Professor
ASME Life Fellow
Mechanical Engineering,
Biomedical Engineering,
and Institute for Complex
Engineered Systems,
Carnegie Mellon University,
Pittsburgh, PA 15213-3890
e-mail: camon@cmu.edu

Blood flow dynamics under physiologically realistic pulsatile conditions plays an important role in the growth, rupture, and surgical treatment of intracranial aneurysms. The temporal and spatial variations of wall pressure and wall shear stress in the aneurysm are hypothesized to be correlated with its continuous expansion and eventual rupture. In addition, the assessment of the velocity field in the aneurysm dome and neck is important for the correct placement of endovascular coils. This paper describes the flow dynamics in two representative models of a terminal aneurysm of the basilar artery under Newtonian and non-Newtonian fluid assumptions, and compares their hemodynamics with that of a healthy basilar artery. Virtual aneurysm models are investigated numerically, with geometric features defined by $\beta=0$ deg and $\beta=23.2$ deg, where β is the tilt angle of the aneurysm dome with respect to the basilar artery. The intra-aneurysmal pulsatile flow shows complex ring vortex structures for $\beta=0$ deg and single recirculation regions for $\beta=23.2$ deg during both systole and diastole. The pressure and shear stress on the aneurysm wall exhibit large temporal and spatial variations for both models. When compared to a non-Newtonian fluid, the symmetric aneurysm model ($\beta=0$ deg) exhibits a more unstable Newtonian flow dynamics, although with a lower peak wall shear stress than the asymmetric model ($\beta=23.2$ deg). The non-Newtonian fluid assumption yields more stable flows than a Newtonian fluid, for the same inlet flow rate. Both fluid modeling assumptions, however, lead to asymmetric oscillatory flows inside the aneurysm dome.

Keywords: non-Newtonian fluid, computational fluid dynamics, intracranial aneurysm, shear stress, pressure

Introduction

Intracranial aneurysms are lesions of the arterial wall commonly located at branching points of the major arteries coursing through the subarachnoid space, predominantly at the circle of Willis in the base of the brain. Aneurysms of the posterior circulation of the circle of Willis are most frequently located at the bifurcation of the basilar artery or at the junction of a vertebral artery and the ipsilateral posterior cerebellar artery. The most common form of intracranial aneurysms is the saccular type [1].

The rupture of an intracranial aneurysm produces a subarachnoid hemorrhage (SAH) associated with high mortality and morbidity rates, as SAH accounts for 1/4 of cerebrovascular deaths. The rupture rate of asymptomatic small aneurysms is only 0.05% per annum in patients with no prior SAH, but increases to 0.5% for large (>10 mm diameter) aneurysms [2]. Aneurysms may be treated by surgical clipping or by interventional neuroradiology, and surgical clipping of asymptomatic aneurysms has morbidity and mortality rates of 10.9% and 3.8%, respectively [2]. Treatment of aneurysms by Guglielmi coils carries 4% morbidity and 1% mortality, but only achieves complete aneurysm occlusion in 52–78% of the cases [2]. According to a recent randomized multicenter trial, endovascular coiling carries a better outcome than neurosurgical clipping for ruptured aneurysms in terms of survival free of disability at 1 year [3]. The management of unruptured intracranial aneurysms is more controversial; the risks associated with their surgical or endovascular repair based on 5 y cumulative rupture rates often depend more on factors such as location, size, age-specific patient risks, etc., rather than the periprocedural complications of the treatment chosen [4]. These treatments promote blood coagulation inside the aneurysm avoiding impinging blood flow on the vessel wall and, thus, impeding its rupture [2,5]. Alteration of blood flow to the inflow zone is used in lesions that are unsuitable for clipping or coil embolization. This strategy is based on the premise that aneurysm expansion and rupture are functions of the fluid shear stress at the flow inlet region. If the flow into the aneurysm can be altered such that the inlet shear stress is reduced, it may be possible to alter the history of the lesion [6].

The pathogenesis and causes for expansion and eventual rupture of saccular aneurysms are not clear. It is generally accepted that unique structural features of the cerebral vasculature contribute to the genesis of these aneurysms. A typical saccular aneurysm has a very thin tunica media and the internal elastic lamina is absent in most cases [1]. Thus, the arterial wall is composed of only intima and adventitia. Consequently, hemodynamics factors, such as blood velocity, wall shear stress, pressure, particle residence time, and flow impingement, play important roles in the pathogenesis of aneurysms and thrombosis. Previously, we have reported on the effect of geometry and transient flow dynamics on the distribution of flow-induced stresses in fusiform and asymmetric virtual aneurysms [7–10]. Aneurysm hemodynamics is contingent on the aneurysm geometry and its relation to the parent vessel, its volume and aspect ratio (depth/neck width) [11]. For this reason, studies of flow dynamics inside models of saccular aneurysms are important to obtain quantitative criteria for their treatments.

Liou and Liou [12] presented a review of in vitro studies of hemodynamics characteristics in terminal and lateral aneurysm models. They reported that with uneven branch flow, the flow dynamics inside a terminal aneurysm and the shear stresses acting on the intra-aneurysmal wall increase proportionally with the bifurcation angle. Imbesi and Kerber [13] have used in vitro models

to study the flow dynamics in a wide-necked basilar artery aneurysm. They investigated the flow after placement of a stent across the aneurysm neck and after placement of Guglielmi detachable coils inside the aneurysm sac through the stent.

Lieber et al. [14] used particle image velocimetry to study the influence of stent design on the flow in a lateral saccular aneurysm model, showing that stents can induce favorable changes in the intra-aneurysmal hemodynamics. Tateshima et al. [15–17] studied the intra-aneurysmal flow dynamics in acrylic models obtained using three-dimensional computerized tomography angiography. They showed that the axial flow velocity structures were dynamically altered throughout the cardiac cycle, particularly at the aneurysm neck. Although aneurysm rupture is thought to be associated with a significant change in aneurysm size, there is still great controversy regarding the size at which rupture occurs. Rupture occurs most frequently at the site of the dome, particularly in daughter aneurysms [15–17]. The relationship between geometric features and rupture is closely associated with low flow conditions; the stagnation of blood flow in large aneurysms is commonly observed with the use of cerebral angiography and is related to intra-aneurysmal thrombosis [18]. Aneurysm geometry often dictates the success of coil embolization. Jou and colleagues [19] presented a compartment model for the estimate of intra-aneurysmal flow and hemodynamic forces that can be used to predict the outcome of coil embolization or possible aneurysm recurrence. Large basilar aneurysms can benefit from a computational fluid dynamics (CFD) approach combined with MR angiography to determine alterations in the flow field caused by the choice of interventional treatment [20].

Foutrakis et al. [21] report on two-dimensional simulations of fluid flow in curved arteries and arterial bifurcations and the relationship to aneurysm formation and expansion. They suggest that the shear stress and pressure developed along the outer wall of a curved artery and at the apex of an arterial bifurcation create a hemodynamics state that can promote aneurysm formation. Recently, Steinman et al. [22] presented image-based computational simulations of the flow dynamics in a giant anatomically realistic human intracranial aneurysm. Their analysis revealed high speed flow entering the aneurysm at the proximal and distal ends of the neck, promoting the formation of persistent and transient vortices within the aneurysm sac. Cebral et al. [23] developed a methodology for modeling patient-specific blood flows in cerebral aneurysms that combines medical image analysis and CFD. The flow analysis in six intracranial aneurysms revealed complex unsteady flow patterns.

Arterial compliance contributes to the mechanical loading and progressive expansion of a blood vessel [24]. This effect has not been considered in the reported studies of hemodynamics in arteries with cerebral aneurysms. The compliant aneurysm wall, which must withstand arterial blood pressure, is composed of layered collagen. Wall strength is related to both collagen fiber strength and orientation. The main characteristic of the aneurysm wall is its multidirectional collagen fibers; with physiological pressures, they become straight and thereby govern the overall stiffness of the lesion [25]. Fluid shear stress modulates endothelial cell remodeling via realignment and elongation, and the time variation of wall shear stress affects significantly the rates at which endothelial cells remodel [26]. Zhao et al. [27] have studied the flow in a carotid arterial bifurcation model with rigid and compliant walls. Generally, there is a reduction in the magnitude of wall shear stress with a compliant wall, with the degree of reduction dependent on the location and phase of the cardiac motion. The local differences, however, are not significant.

The influence of non-Newtonian properties of blood on the arterial flow was investigated by Gijsen et al. [28]. They performed laser Doppler anemometry experiments and finite element simulations of steady flow in a three-dimensional model of the carotid bifurcation. A comparison between the experimental and numerical results showed good agreement for both Newtonian and non-Newtonian fluids. Ma et al. [29] have recently performed a three-dimensional geometrical characterization of cerebral aneurysms from computed tomography angiography data, reconstructing the geometry of nonruptured human cerebral aneurysms. This geometry can be classified as hemisphere, ellipsoid, or sphere; it is apparent that quantified aneurysm shape is more effective than size indices in discriminating between ruptured and unruptured aneurysms [30]. Parlea et al. [31] presented a relatively simple approach to characterizing the simple-lobed aneurysm shape and size using angiographic tracings. Their measurements characterize the range of shapes and sizes assumed by these lesions, providing useful guidelines for the development of models for numerical investigation of hemodynamics in cerebral aneurysms.

In this work, we present detailed numerical simulations of three-dimensional unsteady flows in two virtual saccular aneurysm models and one healthy model of the basilar artery. The computational geometries were developed with representative dimensions as reported in [31]. The purpose of this manuscript is to report on the effects of aneurysm geometry and non-Newtonian blood properties on the flow characteristics, wall pressure and wall shear stress, and to establish comparisons of these flow variables with a healthy basilar artery. This investigation provides valuable insight in the study of statistically representative saccular aneurysms subject to physiologically realistic pulsatile loads.

Mathematical and Numerical Modeling

Governing Equations. The mass and momentum conservation equations for an incompressible fluid can be written as

$$\nabla \cdot \mathbf{v} = 0 \tag{1}$$

$$\rho\left(\frac{\partial \mathbf{v}}{\partial t} + \mathbf{v} \cdot \nabla \mathbf{v}\right) = -\nabla p + \nabla \cdot \boldsymbol{\tau} \tag{2}$$

where ρ is the density, $\mathbf{v}$ is the velocity field, p is the pressure, and τ is the deviatoric stress tensor. This tensor is related to the strain rate tensor; however this relation is usually expressed as an algebraic equation of the form

$$\tau = \mu\dot{\gamma} \tag{3}$$

where μ is the viscosity and $\dot{\gamma}$ is the strain rate, which is defined for incompressible fluid as

$$\dot{\gamma} = \left(\frac{\partial v_i}{\partial x_j} + \frac{\partial v_j}{\partial x_i}\right) \tag{4}$$

For the Newtonian fluid assumption the viscosity of blood is constant and a typical value of $\mu = 3.19$ cP was used. However, blood is a suspension of red blood cells in plasma. The viscosity of blood is mainly dependent on the volume fraction of red blood cells in plasma. The Herschel-Bulkley fluid model of blood assumes that the viscosity μ varies according to the law

$$\mu = k\dot{\gamma}^{n-1} + \frac{\tau_o}{\dot{\gamma}} \tag{5}$$

The Herschel-Bulkley fluid model of blood extends the simple power law model for non-Newtonian fluids to include the yield stress τ_o. Like the Casson model, it shows both yield stress and shear-thinning non-Newtonian viscosity, and it is an accurate model to describe the rheological behavior of blood [32]. We have taken the experimental values recommended by Kim [33] as $k = 8.9721$ cPs^{n-1}, $n = 0.8601$, and $\tau_o = 17.5$ mPa. The density of blood is assumed constant, $\rho = 1050$ kg/m^3, for both Newtonian and non-Newtonian fluid assumptions.

Model Geometry and Boundary Conditions. Figure 1 shows the geometry of our basilar artery models in the cases of a healthy bifurcation and with a saccular aneurysm. Aneurysm model 1, shown in Fig. 1(b), is a saccular symmetric aneurysm with $\beta = 0$ deg, and aneurysm model 2, shown in Fig. 1(c), is an asym-
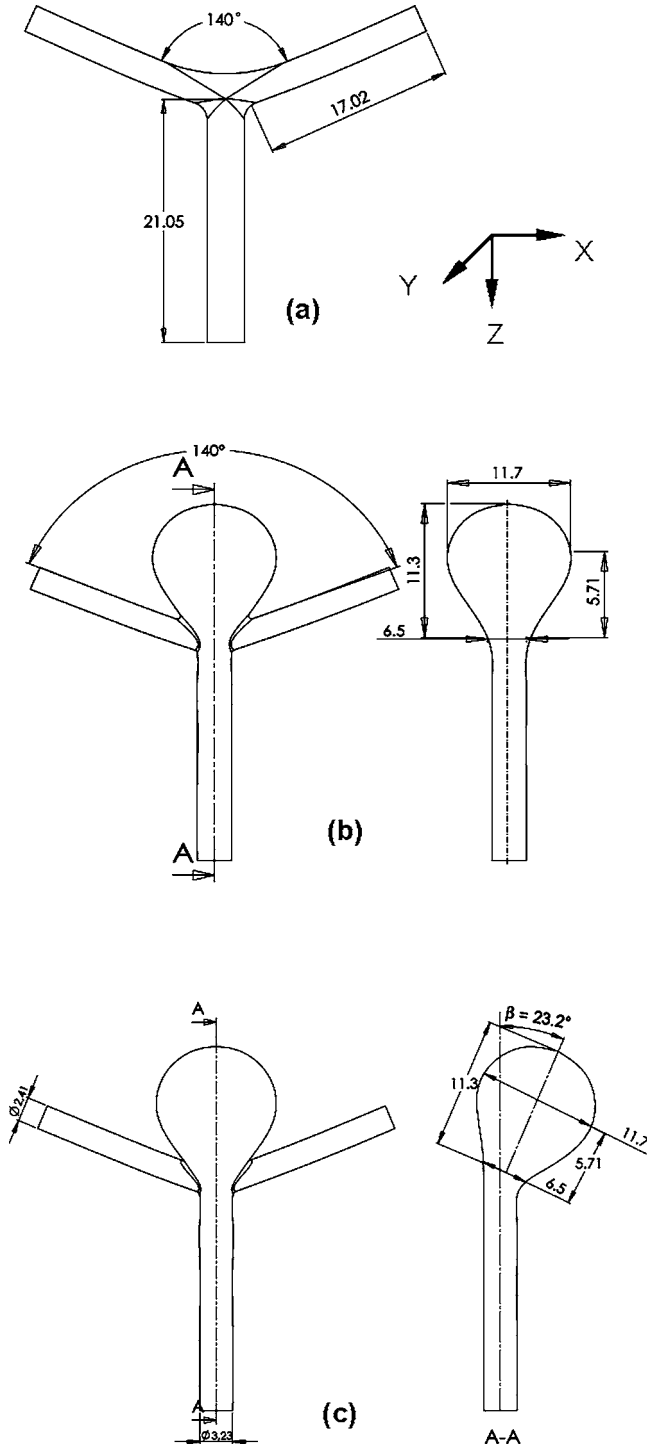
Fig. 1 Model geometries (all dimensions in mm): (*a*) Healthy basilar artery model, (*b*) aneurysm model 1 – with $\beta=0$ deg, (*c*) aneurysm model 2 – with $\beta=0$ deg

Fig. 2 Physiological waveform of mean inlet velocity (U_m) in m/s

metrical aneurysm at an angle $\beta=23.2$ deg. The angle β indicates the tilt of the aneurysm dome with respect to the parent vessel. Physiologically, the bifurcation geometry and aneurysm location exhibit a great amount of irregularity and asymmetry. Average values of neck width, dome height, dome diameter, semi-axis height, basilar artery diameter, and typical β angles of saccular aneurysms of the basilar artery were obtained from the measurements reported by Parlea et al. [31], where $\beta=23.2$ deg corresponds to the standard deviation of the cases analyzed by these
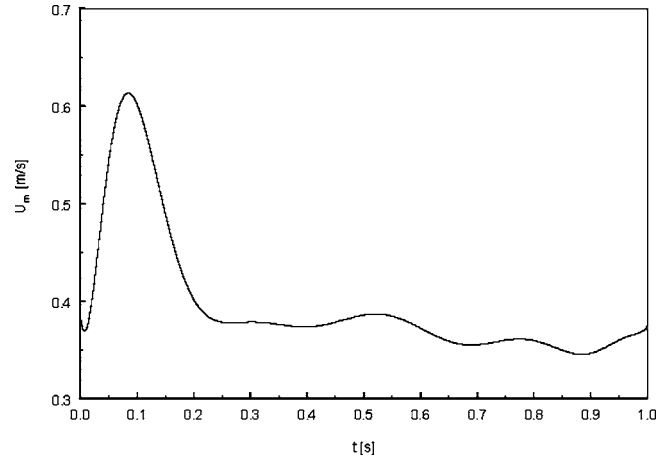
authors. The bifurcation angle between the basilar and the posterior cerebral arteries was taken as 140 deg, also used by Liou et al. [12]. The lengths of the arteries are 6.5 and 7.1 times the respective artery diameters for the basilar and posterior cerebral arteries, so that the velocity boundary conditions were imposed distant from the aneurysm location.

The mean blood flow rate in the basilar artery is 195 mL/min as reported in [34] for healthy human subjects. With $d=3.23$ mm, we obtain a mean blood velocity in the basilar artery of 39.7 cm/s. We also consider a reduction of diameter for the posterior cerebral arteries as 0.75 times the basilar artery diameter. With this reduction the mean flow velocity in the posterior cerebral arteries is 35.6 cm/s; this value is very similar to the mean velocity of 36.0 cm/s reported in [35] for the posterior cerebral artery in normal patients.

The blood flow waveform in arteries of the anterior circulation of the circle of Willis has been studied in detail. Holdsworth et al. [36] have characterized the waveform of the common carotid artery in normal human subjects. However, a detailed measurement of the velocity waveform in the basilar artery is not available. It is difficult to perform Doppler ultrasound measurements in this region of the posterior circulation of the circle of Willis. Schweizer et al. [37] reported a pulsatility index Pi=0.8 and resistance index Ri=0.5 for the basilar artery in healthy volunteers. Baumgartner et al. [38] have measured PV=67 cm/s and ED=29 cm/s in the basilar artery for normal subjects. Figure 2 shows the representative physiological waveform of the mean velocity at the inlet of the basilar artery as used in the present work. We have taken PV=61 cm/s, MV=39.7 cm/s, and ED=35 cm/s. The time dependency of the inflow mean velocity is imposed by a polynomial representation of order 13 and the natural frequency of the pulsatile flow is set to $f=1.0$ Hz. The Womersley number, which characterizes the flow frequency, the geometry of the model and the fluid viscous properties, is $\alpha=2.32$. Peak systolic flow occurs at $t=0.09$ s. The time-averaged Reynolds number with the Newtonian fluid assumption is $\mathrm{Re}_m=422$. The equivalent Reynolds number defined for a Herschel-Bulkley non-Newtonian fluid model with $\tau_0=0$ is
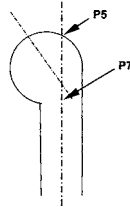
$$\mathrm{Re}_m = \frac{\rho U^{2-n} d^n}{\left[\dfrac{8^{n-1} k(3n+1)}{4n}\right]^n} \qquad (6)$$

and it yields $\mathrm{Re}_m=380$, which is 10% lower than the Reynolds number for Newtonian fluid.

For all models, the boundary condition for the inlet velocity is defined by Eq. (7):

Table 1 Mesh refinement comparisons for two characteristic times at points P5 and P7

Mesh ID	Grid size [cells]	v_z [cm/s] t=0.09 s	v_z [cm/s] t=0.8 s	p_w [mmHg] t=0.09 s	p_w [mmHg] t=0.8 s	WSS [dyn/cm^2] t=0.09 s	WSS [dyn/cm^2] t=0.8 s
A	51,150	55.0	35.0	0.23	0.09	16.7	13.8
B	106,513	62.1	38.5	0.32	0.11	24.0	18.1
C	170,828	61.0	37.2	0.27	0.09	21.7	16.6
D	211,435	62.1	38.0	0.26	0.09	22.1	17.0
E	252,716	62.7	39.2	0.29	0.10	20.5	15.9
F	404,068	65.0	40.2	0.25	0.08	21.5	17.2
G	701,431	64.0	39.6	0.35	0.12	23.6	18.1
H	1,022,382	64.5	40.5	0.30	0.10	23.9	18.5

Fig. 3 Representative computational grid used for aneurysm model 2 (β=23.2 deg)

$$\Delta t = \frac{\Delta x^2}{2(\mu/\rho) + U\Delta x} \tag{8}$$

Unstructured grids of 84,318 cells were used for the healthy models. The models with terminal aneurysms were meshed with 212,541 and 211,435 cells for β=0 deg and β=23.2 deg, respectively. The same grid size was used for the Newtonian and non-Newtonian blood assumptions. The unstructured grids were composed of tetrahedral elements as shown in Fig. 3 for aneurysm model 2. Although the geometry of model 1 is symmetric, the resulting unstructured mesh is not symmetric with respect to the longitudinal axis of the model.

A computational study on mesh sensitivity and discretization, and the numerical integration method is performed to determine the "best" computational mesh and solution scheme for reasonable CPU solution times. The mesh sensitivity study considers eight (8) different discretizations of aneurysm model 2 ranging from 51,150 cells for the coarser grid size to 1,022,382 cells for the finer grid size as shown in Table 1. This table shows numerical results for the streamwise velocity (v_z) at point P7, and the relative wall pressure (p_w) and wall shear stress (WSS) at point P5, the instantaneous systolic and diastolic times t=0.09 s and t=0.8 s as indicated in the schematic below the table. The variation of v_z with grid size is shown in Fig. 4, illustrating an asymptotic behavior as the number of cells is increased. Least square fits with exponential functions were used to describe this behavior of the three variables to find an independent mesh solution as the number of cells was increasingly doubled. The following exponential equation was used to fit the numerical data of v_z, p_w, and WSS, as a function of mesh size: $(v_z, p_w, \text{WSS}) = A_o + B_o \cdot e^{C_o \cdot N_c}$, where A_o, B_o, and C_o, are constants calculated using the data for each mesh

$$U(t) = U_m(t) \cdot \frac{3n+1}{n+1}\left[1 - \left(\frac{r}{a}\right)^{\frac{n+1}{n}}\right] \tag{7}$$

where n=1 for a Newtonian fluid, n=0.8601 for the Herschel-Bulkley non-Newtonian fluid model, and $U_m(t)$ is given by the flow waveform illustrated in Fig. 2. The time-dependent parabolic velocity profile of Eq. (7) is used as a boundary condition at the computational domain inlet, after performing comparisons between the parabolic velocity profile and the Womersley solution velocity profile for a Newtonian flow in a straight pipe [39]. These comparisons have the objective of determining the accuracy and properness of the parabolic profile. Equation (7) is more easily implemented in the computational code than the Womersley solution profile. The velocity profile is imposed at a distance of 21 mm from the entrance of the aneurysm and, therefore, the flow becomes fully developed before entering the aneurysm sac. Actual cerebral aneurysms have a basilar artery longer than 21 mm. In addition, although the basilar artery receives blood from both left and right vertebral arteries, it is long enough to allow both flow streams to mix yielding a near parabolic shaped velocity profile, which should change continuously in the axial direction with the pulsatility of the flow. The outflow boundary condition is defined by $\partial \phi / \partial \mathbf{n}$=0 for the fluid velocity (ϕ=**V**) at the exit of each posterior cerebral artery and the flow rates for each artery are identical. A no-slip condition is prescribed at the walls.

Numerical Method. Governing Eqs. (1)–(5) were solved with the software FLUENT (v6.0, Fluent, Inc., Lebanon, NH), which utilizes the finite volume method for the spatial discretization. The interpolations for velocities and pressure are based on power-law and second order, respectively. The pressure-velocity coupling is obtained using the SIMPLEC algorithm. The explicit time-marching second order scheme with a time step Δt=2×10^{-5} s was used for the transient computations. The numerical solution is adjusted at each time step based on the computation of pressures relative to a chosen arbitrary reference of 45 mmHg (the typical amplitude of an intraluminal basilar pressure waveform) located at point P7, on the aneurysm entrance cross-section, as shown schematically on the inset of Table 1. The time step was computed from the Courant-Levy condition [40] as given by Eq. (8). With this small time step the residual of the continuity and Navier-Stokes equations were smaller than 10^{-5} in all temporal iterations.
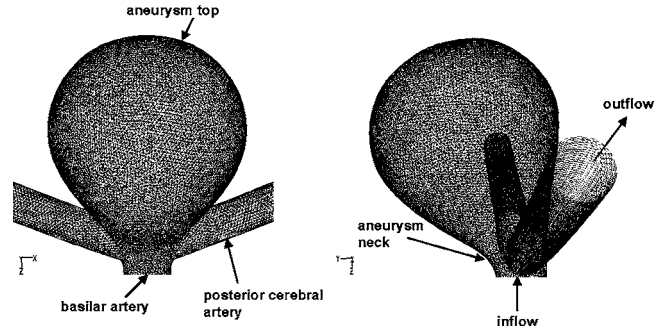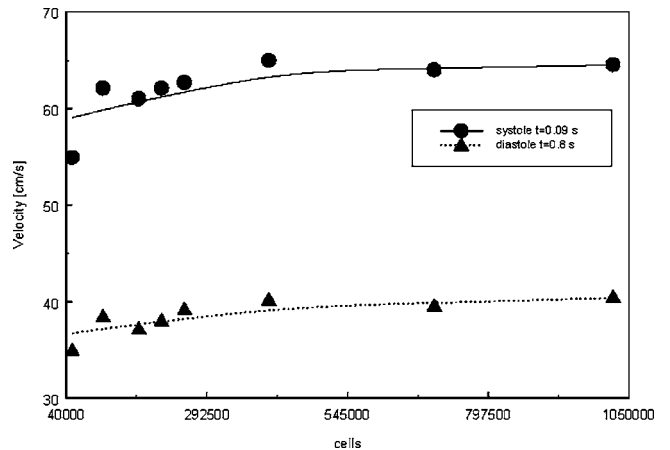

Fig. 4 Axial velocity versus grid size for two instantaneous times at point P7
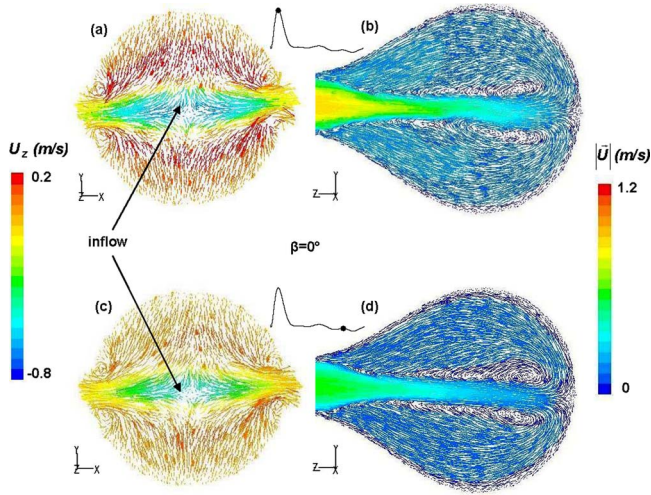
Fig. 5 Velocity vectors for aneurysm model 1 (β=0 deg) and non-Newtonian fluid color-coded with the *z*-component of the velocity for (*a*) *t*=0.1 s and (*c*) *t*=0.8 s at the aneurysm inlet, and color-coded with the velocity magnitude for (*b*) *t*=0.1 s and (*d*) *t*=0.8 s at the *Y-Z* plane of the aneurysm

Fig. 6 Velocity vectors for aneurysm model 2 (β=23.2 deg) and non-Newtonian fluid color-coded with the *z*-component of the velocity for (*a*) *t*=0.1 s and (*c*) *t*=0.8 s at the aneurysm inlet, and color-coded with the velocity magnitude for (*b*) *t*=0.1 s and (*d*) *t*=0.8 s at the *Y-Z* plane of the aneurysm

used in this investigation, and Nc is the number of cells in each mesh. It can be shown that the primary variable, v_z, experiences a variation between meshes D and H of 4% and 6% for times t =0.09 s and t=0.8 s, respectively. The other variables, p_w and WSS, also present an asymptotic behavior proportional to the increase in number of cells. The difference in WSS between meshes D and H is 8% for both systole and diastole. The difference in relative wall pressure between these meshes is 15.4% and 11.1% for t=0.09 s and t=0.8 s, respectively. However, considering the reference pressure for the domain located at P7, these relative pressure fluctuations in the mesh sensitivity analysis become negligible. Furthermore, a qualitative comparison of WSS and p_w patterns for t=0.09 s and t=0.8 s on the entire computational domain for aneurysm models 1 and 2 reveals no significant variation for meshes D to H. In addition, a comparison of CPU times for meshes D to H based on three pulsatile flow cycles shows that mesh H is 3.2 times more computationally expensive than mesh D, while obtaining an improvement of about 6% in the streamwise v_z-velocity at point P7. Thus, the results obtained with mesh D are those presented in this manuscript, since 211,435 cells is refined enough for a reasonable accuracy and CPU solution time. The workstation used to perform the simulations is based on an Intel Pentium IV processor of 2.8 GHz clock speed, 1.5 Gb RAM memory and runs on the Linux Redhat v8.0 operating system. A typical simulation time based on 3 consecutive pulsatile flow cycles employing 1.5×10^5 iterations was approximately 320 CPU hours.

Results

Flow Dynamics. The non-Newtonian flow characteristics for aneurysm models 1 and 2 are shown in Figs. 5 and 6, respectively, at two regions of the aneurysm: the aneurysm neck in a plane perpendicular to the basilar artery (*X-Y* plane) and a plane parallel to the basilar artery longitudinal axis (*Y-Z* plane).

The inflow and outflow regions at the aneurysm neck are illustrated in Figs. 5(*a*) and 5(*c*) for model 1 (β=0 deg) and in Figs. 6(*a*) and 6(*c*) for model 2 (β=23.2 deg) in the *X-Y* plane. For representation purposes the same scale for velocity vectors is used in both models for U_z and $|\vec{U}|$. High velocity flow dominates the vortex dynamics at peak systole (t=0.1 s) with a jet of fluid traveling through the center of the aneurysm for model 1 and sym-
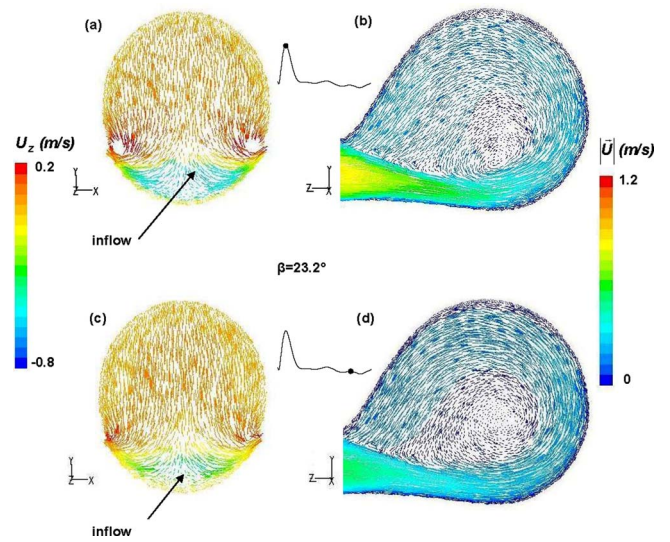
metrically bifurcating in two streams communicating with the posterior cerebral arteries. The asymmetry of the dome in model 2 yields a high velocity jet through the outflow regions and shears the lower wall of the aneurysm with retrograde flow. At a typical diastolic time (t=0.8 s), the flow patterns in both models remain unaltered in their structure, only decreasing the mean velocity at every location. Figures 5(*b*) and 5(*d*) for aneurysm model 1 and Figs. 6(*b*) and 6(*d*) for aneurysm model 2 show the intra-aneurysmal flow in the *Y-Z* plane. For model 1, the intra-aneurysmal flow shows a nearly symmetric flow dynamics with a ring vortex enclosing the centerline jet, represented by two vortices in this view. The asymmetry of the vortices with respect to centerline holds for the systole-diastole cycle, defining a well established stagnation zone where the jet impinges on the wall and where high wall pressure is expected. This asymmetry is also anticipated because 3D flows can generate instabilities to relatively low Reynolds numbers, despite the fact that the body forces are negligible due to the small dimensions of the aneurysm. The asymmetry of the geometry for model 2 affects the intra-aneurysmal flow by yielding a single recirculation region at the center of the dome. The difference between peak systole [Figs. 5(*b*) and 6(*b*)] and late diastole [Figs. 5(*d*) and 6(*d*)] is observed by the size of the vortical structures, which are larger and slower at t=0.8 s. The two aneurysm models differ in the magnitude of the velocity gradients and wall shear stresses due to the development of flow patterns with vortices and recirculation regions dependent on the particular aneurysm shape. During the systolic phase, higher velocities develop at the inlet region in model 1 than in model 2 as shown in Figs. 5(*a*) and 6(*a*). In model 2 the inlet flow is guided by the shape of the aneurysm, which in turn should diminish the wall pressure and increase the shear stresses on the wall. Regions with U_z higher than 0.2 m/s in model 2 correspond to the outflow region, and they appear as empty regions.

The jet of fluid through the neck of the aneurysm (i.e., inflow region) varies in size and position depending on the tilt of the aneurysm dome with respect to the parent vessel. This finding is important for the endovascular treatment of cerebral aneurysms, since controlling blood flow at the inflow region is a critical step in achieving permanent occlusion of an aneurysm. The long-term anatomical durability of coil embolization in cerebral aneurysms by means of microcoil technology depends on the aneurysm shape
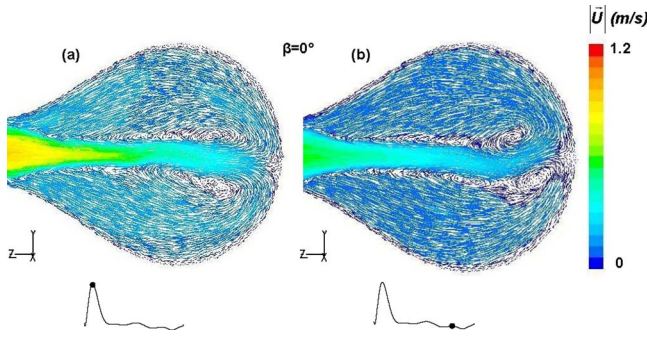
Fig. 7 Velocity vectors for aneurysm model 1 ($\beta=0$ deg) and Newtonian fluid, color-coded with the velocity magnitude for (a) $t=0.1$ s and (b) $t=0.8$ s

Fig. 8 Wall shear stress (WSS) for model 1 ($\beta=0$ deg) with a view from the top of the aneurysm: (a) $t=0.1$ s and (b) $t=0.8$ s, Newtonian fluid; (c) $t=0.1$ s and (d) $t=0.8$ s, non-Newtonian fluid

and the blood flow dynamics at the aneurysm neck. As such, we infer that recanalization will be less likely if the coils are inserted through the inflow region of the aneurysm neck. Therefore, careful consideration of the aneurysm asymmetry with respect to the parent vessel (β) must be taken into account during these endovascular procedures in relation to the resulting flow dynamics at the inflow region.

We next investigate the effect of the Newtonian fluid assumption on the vortex dynamics by comparing with the non-Newtonian flow predictions (Fig. 5) at peak systole and late diastole at the Y-Z plane for aneurysm model 1 (Fig. 7). The vortex structure shows more instability and departure from the symmetry axis than for a non-Newtonian fluid [Figs. 5(b) and 5(d)]. Our results indicate that symmetry breaking and oscillatory flows are related phenomena. Oscillatory flows yield moving vortices, which increase and decrease in size in an oscillatory sinusoidal manner. Increased intra-aneurysmal flow separation is observed at late diastole, Fig. 7(b), leading to multiple vortex structures and asymmetry of the centerline jet. A fluid with a strain rate dependent on viscosity is more stable to the acceleration and deceleration phases of the cardiac cycle. Viscous forces in a non-Newtonian fluid can be large enough to prevent symmetry breaking and oscillatory flows. In this investigation however, the viscous forces are unable to keep the flow symmetry. Additionally, they are larger than in a Newtonian fluid for the same inlet flow rate. These differences are relevant for the assessment of endovascular device performance, which should not be based solely on the hemodynamics of complex arteries with a Newtonian fluid model.

Flow-induced Stresses. Our computational investigations have demonstrated (not reported here) that for aneurysm models 1 and 2, there are small differences in the pressure field for Newtonian and non-Newtonian flow simulations. This is due to the rigid wall assumption of the geometry and as such minimal emphasis is given to p_w in this article. The Newtonian and non-Newtonian characteristics of the wall shear stress (WSS) are shown in Figs. 8 and 9 for aneurysm models 1 ($\beta=0$ deg) and 2 ($\beta=23.2$ deg), respectively, as instantaneous representations of an overhead view of the top of the aneurysm for two typical times at systole and diastole. These representations show clear qualitative and quantitative differences on the spatial WSS distribution between the two types of fluid assumptions. The loss of symmetry of this distribution is more noticeable for the Newtonian fluid than for the non-Newtonian fluid due to the stronger viscous forces resulting from applying the variable viscosity constitutive equation. These forces lead to more stable and less oscillatory flows within both symmetric and asymmetric aneurysms, as in models 1 and 2, respectively.

The top view of aneurysm model 1 shown in Figs. 8(c) and 8(d) for the non-Newtonian fluid, indicates a pattern of quasi-symmetry in the wall shear stresses (and also for wall pressure, not shown). For both flow stages, the highest values of shear
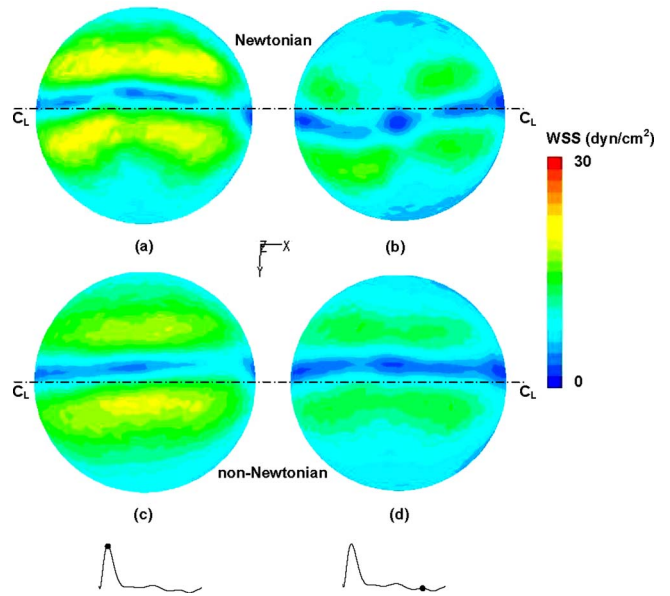
stresses are in regions located almost symmetrically with respect to the imaginary centerline. Thus, regions on the aneurysm wall located closer to the centerline, e.g., point P3 in Fig. 10, will present lower wall shear stresses than regions located further from it, but still in the higher shear stress region, e.g., point P4 in Fig. 10, for the entire pulsatile cycle. As shown in Figs. 9(c) and 9(d) for aneurysm model 2, the highest shear stresses are located asymmetrically with respect to the centerline, e.g., point P5 in Fig. 11, with shear stresses diminishing closer to the centerline, e.g., point P6 in Fig. 11. As in model 1, this pattern of WSS is characteristic of both systole and diastole. Therefore, temporal evolutions of
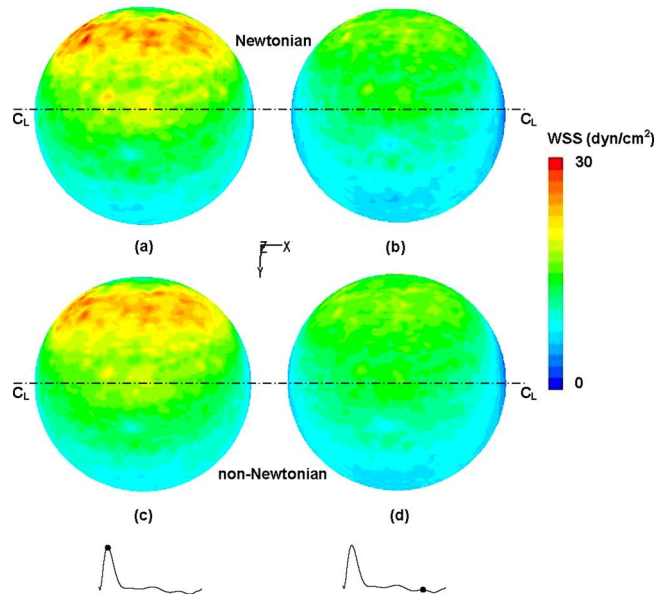

Fig. 9 Wall shear stress (WSS) for model 2 ($\beta=23.2$ deg) with a view from the top of the aneurysm: (a) $t=0.1$ s and (b) $t=0.8$ s, Newtonian fluid; (c) $t=0.1$ s and (d) $t=0.8$ s, non-Newtonian fluid
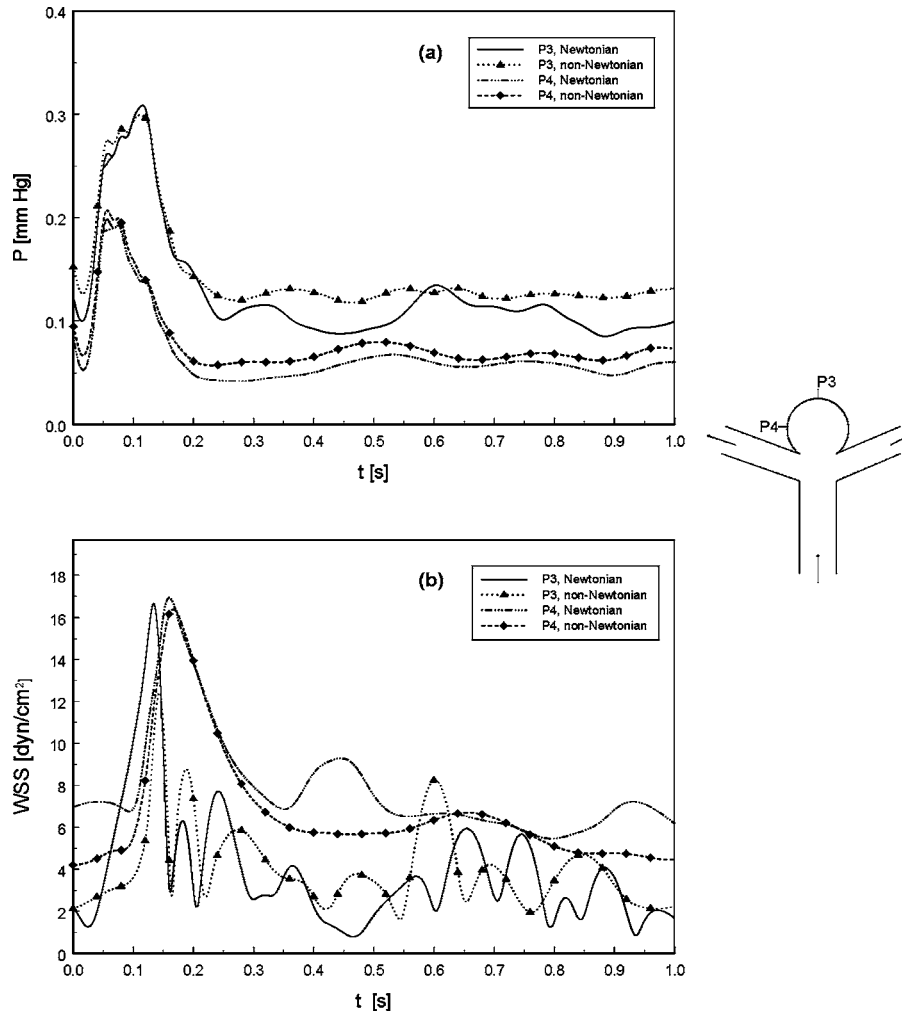
Fig. 10   Flow-induced stresses in aneurysm model 1: (*a*) **Relative wall pressure—p_w and** (*b*) **wall shear stress—WSS at points P3 and P4 on the wall of model 1 ($\beta=0$ deg) in the *X-Z* plane**

WSS should develop a pattern with consistently higher values of shear stresses at points P4 and P5, for symmetric and asymmetric aneurysm shapes, respectively.

The temporal variation of both WSS and p_w at precise locations of the aneurysm is an important variable for obtaining information on the cause of aneurysm wall rupture with respect to the intensity of the stresses and their temporal evolution in sensitive regions. The precise locations are chosen where stagnation points (P1 and P3) and high shear stresses (P2, P4, P5, and P6) are expected.

Figures 12(*a*) and 12(*b*) show the temporal evolution of p_w and WSS for Newtonian and non-Newtonian fluids in two characteristic points of a healthy basilar artery. Both variables closely resemble the inlet velocity waveform (Fig. 2). Evidently, the wall pressure at point P1 is higher than at point P2, since P1 corresponds to a stagnation point, whereas P2 develops a higher wall shear stress than P1 because the velocity gradients are larger downstream of the bifurcation. For this geometric configuration, there is no effect on the magnitude of p_w due to the non-Newtonian nature of the fluid, except during the systolic phase. The wall shear stress for a non-Newtonian fluid decreases at point P2 since the viscous forces are larger for a Newtonian fluid. The temporal evolution of p_w and WSS at two characteristics points for aneurysm model 1, indicated as P3 and P4, for Newtonian and non-Newtonian fluid are shown in Figs. 10(*a*) and 10(*b*), slightly resembling the inlet velocity waveform only during the systolic

phase. These stresses, however, develop strong time oscillations during the diastolic phase of the cycle. In this phase, the temporal variation of wall pressure at P3 and P4 presents an oscillatory pattern, such that p_w at P3 is higher than at P4 since the former is closer to the stagnation point. After peak systole for a non-Newtonian fluid model, the temporal wall pressure is higher at both points than for a Newtonian fluid. During the diastolic phase, p_w at P3 is approximately 25% higher on average with a non-Newtonian fluid model, as the incoming jet always impinges at the same point within the stagnation region. The wall pressure difference at P4 between non-Newtonian and Newtonian fluid models is about 15% on average.

Illustrated in Fig. 10(*b*), the temporal evolution of WSS at P3 and P4 shows a time-dependent oscillatory behavior that does not resemble the inlet velocity waveform. At systole, the maximum WSS for P3 and P4 is nearly the same only for Newtonian fluid. For non-Newtonian fluid, the maximum depends on the location of P3 and P4. However, during diastole, the WSS distribution depends on point location and the viscous characteristics of the fluid model. WSS at P3 is lower than at P4, as P3 is located within the stagnation region where velocity gradients are smaller than at P4. Additionally, P3 presents more time-dependent oscillations during diastole than P4, because within the stagnation region the velocity gradients strongly oscillate regardless of the Newtonian
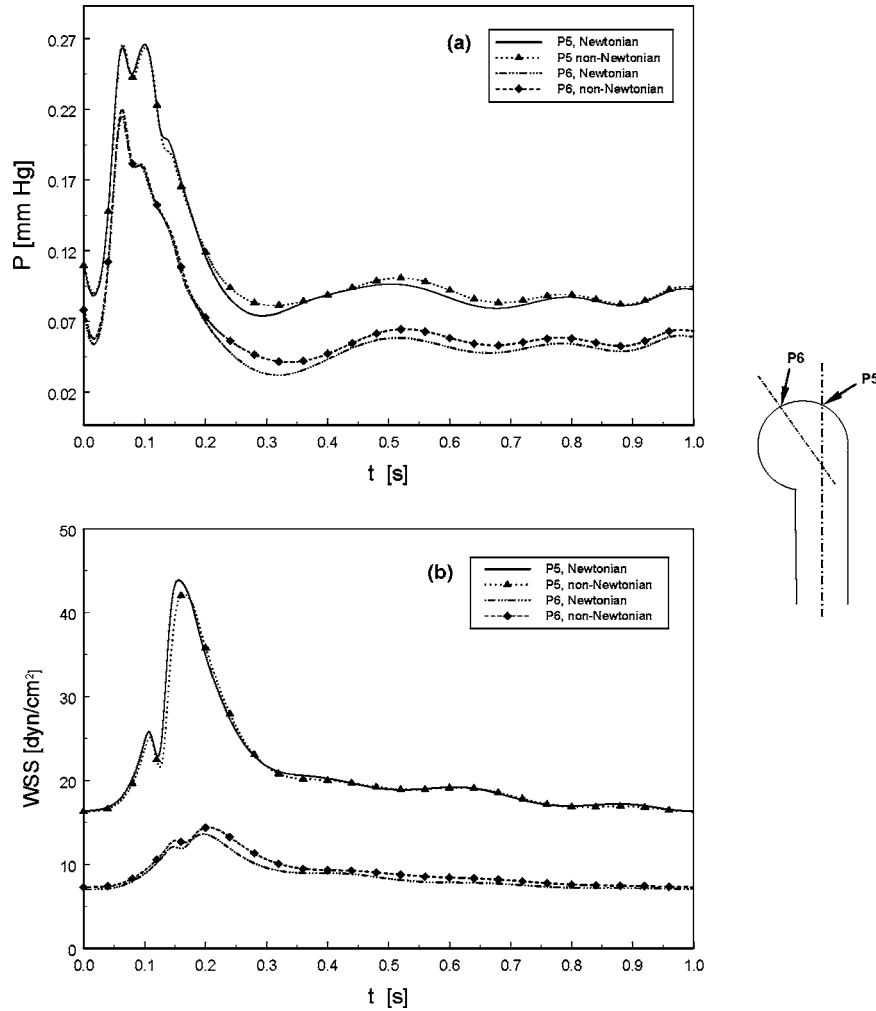
Fig. 11 Flow-induced stresses in aneurysm model 2: (a) Relative wall pressure—p_w and (b) wall shear stress—WSS at points P5 and P6 on the wall of model 2 (β =23.2 deg) in the Y-Z plane

or non-Newtonian nature of the fluid. Thus, the non-Newtonian fluid assumption for model 1 yields stronger viscous forces and a more stable flow with less time oscillations.

To understand the time-dependent behavior of the oscillatory shear stresses during the pulsatile systolic-diastolic blood flow cycle within the aneurysm, numerical simulations are performed with model 1 (β=0 deg) for a constant inlet volumetric flow rate of Q=195 mL/min and Newtonian flow. Figure 13 shows the wall shear stress temporal evolution for point P3. A periodic behavior with a time-period of T=0.057 s is noted, which corresponds to a frequency of f=17.5 s^{-1}. This flow loses its symmetry and oscillates in a sinusoidal manner, which leads to oscillatory wall shear stress at P3. Thus, the time-dependent oscillatory behavior of the wall shear stresses at P3 of aneurysm model 1 for pulsatile inlet flow conditions is caused by both the pulsatile flow itself and the fundamental oscillations that this 3D flow generates within the aneurysm for steady inlet flow conditions. Consequently, the flow field asymmetry observed during pulsatile flow simulations is not only noted in pulsatile flow but also in steady state inlet flow, and it is inherent to instabilities originated in 3D flows at relatively low Reynolds numbers.

Figures 11(a) and 11(b) illustrate the temporal variation of p_w and WSS, respectively, at two characteristic points, P5 and P6, of aneurysm model 2 for Newtonian and non-Newtonian fluid. The distribution of p_w and WSS closely resembles the inlet velocity waveform and their pattern is similar to that of the healthy basilar

artery (Fig. 12). The effect of a non-Newtonian fluid model is almost negligible during the entire cardiac cycle since in this aneurysm geometry the flow is more stable than in model 1, regardless of the relatively larger viscous forces developed with a non-Newtonian fluid. Since the flow in model 2 is lead to the dome by the shape of the aneurysm wall, there is no jet impinging on the wall, but rather an extensive region where the wall pressure is higher. Thus, p_w and WSS are lower at P6, as this point is relatively far from the region of higher pressure and velocity gradients.

A comparison of the two saccular aneurysms with the healthy basilar artery model [P1 in Fig. 12(a)] reveals a reduction in wall pressure at peak systole of 88% for model 1 [P3 in Fig. 10(a)] and 90% for model 2 [P5 in Fig. 11(a)] for either a Newtonian or non-Newtonian fluid. Similarly, peak WSS is reduced by 73% in model 1 and by 7% in model 2 at peak systole for a non-Newtonian fluid; for a Newtonian fluid, these differences are 64% and 6%, respectively. From this comparison we infer that the effect of geometry represented by the asymmetry parameter β, has a stronger effect on the relative magnitude of the flow-induced stresses than the assumption of blood as a fluid with variable viscosity. The low-velocity conditions generated by the presence of the saccular aneurysms also produce a phase-lag in achieving peak systole within the dome, as maximum WSS is obtained for $t>0.1$ s at the specific points illustrated in Figs. 10(b) and 11(b).
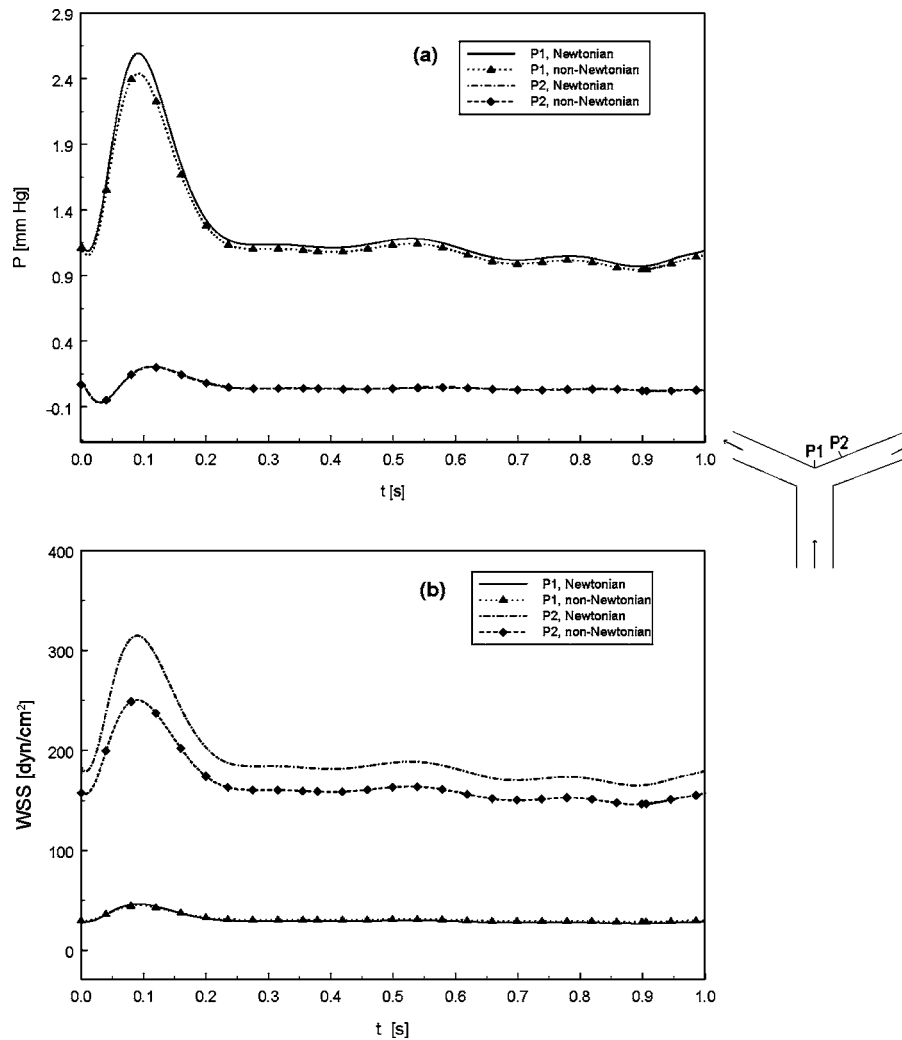
Fig. 12 Flow-induced stresses in the healthy basilar artery model: (*a*) Relative wall pressure −p_w and (*b*) wall shear stress—WSS at points P1 and P2 on the wall of the healthy basilar artery bifurcation

Discussion

Observations on Wall Shear Stress. Several authors have reported the importance of the WSS on the development, growth and rupture of cerebral aneurysms [22,41]. High wall shear stress is regarded as a major factor in the development and growth of cerebral aneurysms. The endothelium is sensitive to changes in WSS and regulates local vascular tone by releasing vasodilator and vasoconstrictor substances [15]. Aneurysm rupture is related to a low level of WSS and, therefore, it is associated with low-flow conditions [42]. Localized stagnation of blood flow is known to result in the aggregation of red blood cells, as well as the accumulation and adhesion of both platelets and leukocytes along the intimal surface. This occurs due to dysfunction of flow-induced nitric oxide, which is usually released by mechanical stimulation through increased shear stress. These factors may cause intimal damage, lead to small thrombus formation and infiltration of white blood cells and fibrin inside the aneurysm wall [18]. Damage to the endothelium is typically hypothesized as a contributing cause of aneurysm growth and rupture. Once the integrity of this layer of cells lining the lumen is breached, subsequent deterioration of the structural fibers of the vessel may occur. Blood flow dynamics is involved in the process leading to vessel remodeling due to wall injury. It is assumed that a WSS of approximately 20 dyn/cm^2 is suitable for maintaining the structure

of the aneurysmal wall and a lower WSS will degenerate endothelial cells [42]. Our results of WSS show values lower than 20 dyn/cm^2 in large parts of the aneurysmal wall over one cardiac cycle. This low WSS may be an important factor underlying the degeneration, indicating the structural fragility of the aneurysmal wall. We hypothesize that the small wall pressure fluctuations observed for both aneurysm models will play a role in the further expansion and ultimate rupture of the aneurysms subsequent to degeneration of the wall structure due to low fluid shear. The effects of WSS and p_w can be examined further by modeling the compliant properties of the aneurysm wall in the continuum.

Another relevant outcome of this investigation is the underlying relationship between the temporal distributions of WSS and p_w on the aneurysmal wall with respect to the flow waveform at the neck of the aneurysm. This is illustrated by the almost constant pressures and shear stresses obtained during diastole for the healthy bifurcation model (Fig. 12) and the asymmetric aneurysm model (Fig. 11), which exhibit more stable flow patterns than the symmetric aneurysm model (Fig. 10) throughout the cardiac cycle. This observation emphasizes the importance of utilizing boundary conditions based on accurate flow measurements in the arteries of the circle of Willis by means of pulsed Doppler ultrasound, a limitation of the present study. The results described in this work provide insight into the flow dynamics and flow-induced wall
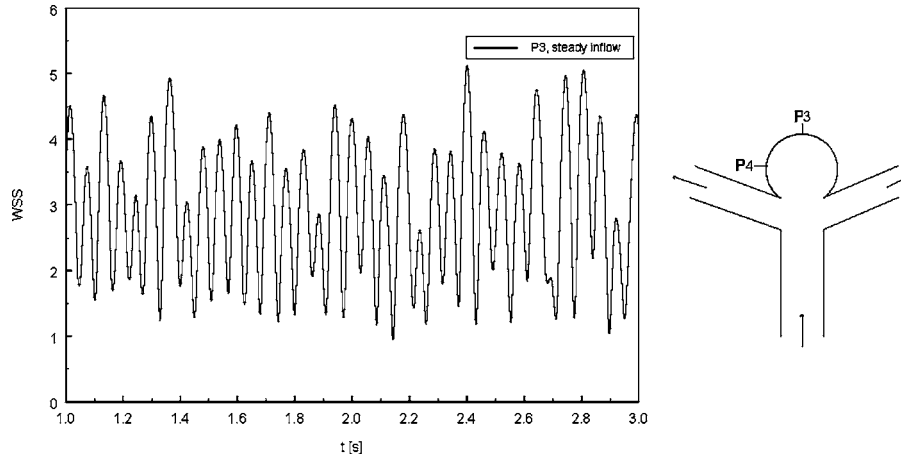
Fig. 13 Temporal evolution of WSS at point P3 in aneurysm model 1 for steady inlet flow rate

stresses in representative geometries of saccular aneurysms with pulsatile inlet flow conditions. Further investigation based on realistic aneurysm physiology is required to reveal which physiological parameters play a role in aneurysm formation.

Limitations. The idealized models utilized in the present study are quite different from patient-specific aneurysms and, therefore, our results should not be extrapolated for their use in realistic anatomies. In particular, the curvature and tortuosity of the parent vessel determine the shape of the velocity profile into the aneurysm, which will, in turn, affect the flow patterns obtained inside the sac. It is expected that in vivo aneurysms located on parent arteries with more curvature would be subjected to higher flow-induced stresses [43] than those reported in this study. In this regard, it is unlikely that a parent vessel geometry as symmetric as those presented here would be encountered in a clinical setting [44]. Nevertheless, transient flows in virtual saccular aneurysms present a complex vortex dynamics that has not been previously described in detail for anatomic reconstructions of patient-specific models [45].

Conclusions

This work presents a numerical investigation of the hemodynamics of two saccular aneurysm models and one healthy model of the basilar artery. The effects of aneurysm shape, asymmetry, and Newtonian/non-Newtonian fluid modeling are studied in detail with respect to flow patterns and the spatial and temporal distributions of wall pressure and wall shear stress.

The flow dynamics in both aneurysm models shows an unsteady and complex vortex structure, and the inflow region varies in size throughout the cardiac cycle. The assessment of such variation should be required during coil embolization of cerebral aneurysms: Recanalization will be less likely when the coils are inserted through the inflow region of the aneurysm neck. Larger spatial and temporal variations of pressure and shear stress are obtained for the wall of the symmetric aneurysm model. At peak systolic flow conditions there is a significant reduction in aneurysm wall pressure and wall shear stress in comparison with a healthy basilar artery. The effect of geometry, assessed by means of the asymmetry parameter β, outweighs the effect of variable blood viscosity on the reduction of these peak flow-induced wall stresses. Further studies are necessary to investigate the effects of arterial compliance on the development, growth, and rupture of patient-specific intracranial aneurysms.

Acknowledgment

Nomenclature

$$
\begin{array}{rl}
a & = \text{basilar artery radius} \\
d & = \text{diameter of basilar} \\
\text{ED} & = \text{end-diastolic velocity} \\
f & = \text{frequency} \\
\text{MV}, U_m & = \text{mean velocity} \\
p & = \text{static pressure} \\
p_w & = \text{relative wall pressure} \\
\text{PV} & = \text{peak flow velocity} \\
\text{Pi} & = \text{pulsatility index} = (\text{PV-ED})/\text{MV} \\
\text{Re} & = \text{Reynolds number} = \rho U_m d/\mu \\
\text{Ri} & = \text{resistance index} = (\text{PV-ED})/\text{PV} \\
T & = \text{time period} \\
u & = \text{velocity} \\
\mathbf{V}_z & = \text{streamwise velocity} \\
\text{WSS} & = \text{wall shear stress}
\end{array}
$$

Greek Symbols

$$
\begin{array}{rl}
\alpha & = \text{Womersley number} = a(2\pi f/\nu)^{1/2} \\
\beta & = \text{angle; tilt of the aneurysm dome with respect} \\
 & \quad \text{to the parent vessel} \\
\dot{\gamma} & = \text{strain rate} \\
\mu & = \text{fluid molecular viscosity} \\
\nu & = \text{fluid kinematic viscosity} = \mu/\rho \\
\rho & = \text{fluid density} \\
\tau & = \text{shear stress} \\
\tau_w & = \text{wall shear stress} \\
\tau_o & = \text{yield stress} \\
\Delta t & = \text{time step}
\end{array}
$$

References

[1] Schievink, W. I., 1997, "Intracranial Aneurysms," N. Engl. J. Med., **336**, pp. 28–40.

[2] Wardlaw, J. M., and White, P. M., 2000, "The Detection and Management of Unruptured Intracranial Aneurysms," Brain, **123**, pp. 205–221.

[3] Molyneux, A., Kerr, R., Stratton, I., Sandercock, P., Clarke, M., Shrimpton, J., and Holman, R.; ISAT Collaborative Group, 2002, "International Subarachnoid Aneurysm Trial (ISAT) of Neurosurgical Clipping Versus Endovascular Coiling in 2143 Patients with Ruptured Intracranial Aneurysms: A Randomized Trial," Lancet, **360**, pp. 1267–1274.

[4] Wiebers, D. O., Whisnant, J. P., Huston, J., III, Meissner, I., Brown, R. D., Jr., Piepgras, D. G., Forbes, G. S., Thielen, K., Nichols, D., O'Fallon, W. M., Peacock, J., Jaeger, L., Kassell, N. F., Kongable-Beckman, G. L., and Torner, J. C., International Study of Unruptured Intracranial Aneurysms Investigators (ISUIA, 2003, "Unruptured Intracranial Aneurysms: Natural History, Clinical Outcome, and Risks of Surgical and Endovascular Treatment," Lancet, **362**, pp. 103–110.

[5] Van Gijn, J., and Rinkel, G. J. E., 2001, "Subarachnoid Haemorrhage: Diagnosis, Causes and Management," Brain, **124**, pp. 249–278.

[6] Hoh, B. L., Putman, C. M., Budzik, R. F., Carter, B. S., and Ogilvy, C. S., 2001, "Combined Surgical and Endovascular Techniques of Flow Alteration to

Treat Fusiform and Complex Wide-Necked Intracranial Aneurysms that are Unsuitable for Clipping or Coil Embolization," J. Neurosurg., **95**, pp. 24–35.

[7] Finol, E. A., and Amon, C. H., 2001, "Blood Flow in Abdominal Aortic Aneurysms: Pulsatile Flow Hemodynamics," ASME J. Biomech. Eng., **123**, pp. 474–484.

[8] Finol, E. A., Keyhani, K., and Amon, C. H., 2003, "The Effect of Asymmetry in Abdominal Aortic Aneurysms Under Physiologically Realistic Pulsatile Flow Conditions," ASME J. Biomech. Eng., **125**, pp. 207–217.

[9] Shkolnik, A. D., Scotti, C. M., Amon, C. H., and Finol, E. A., 2005, "Computational Modeling of Abdominal Aortic Aneurysms: An Assessment of Rupture Potential for Presurgical Planning," in *Biomechanics Applied to Computer Assisted Surgery*, Payan, Y. ed., Research Signpost publisher, Kerala, India, pp. 243–260.

[10] Scotti, C. M., Shkolnik, A. D., Muluk, S. C., and Finol, E. A., 2005, "Fluid-Structure Interaction in Abdominal Aortic Aneurysms: Effects of Asymmetry and Wall Thickness," Biomed. Eng. Online, **4**(64).

[11] Weir, B., Amidei, C., Kongable, G., Findlay, J. M., Kassell, N. F., Kelly, J., Dai, L., and Karrison, T. G., 2003, "The Aspect Ratio (dome/neck) of Ruptured and Unruptured Aneurysms," J. Neurosurg., **99**, pp. 447–451.

[12] Liou, T. M., and Liou, S. N., 1999, "A Review on in vitro Studies of Hemodynamic Characteristics in Terminal and Lateral Aneurysm Models," *Proceedings of the National Science Council, Republic of China, Part B, Life Sciences*, 23, pp. 133–148.

[13] Imbesi, S. G., and Kerber, C. W., 2001, "Analysis of Slipstream Flow in a Wide-Necked Basilar Artery Aneurysm: Evaluation of Potential Treatment Regimens," AJNR Am. J. Neuroradiol., **22**, pp. 721–724.

[14] Lieber, B. B., Livescu, V., Hopkins, L. N., and Wakhloo, A. K., 2002, "Particle Image Velocimetry Assessment of Stent Design Influence on Intra-Aneurysmal Flow," Ann. Biomed. Eng., **30**, pp. 768–777.

[15] Tateshima, S., Murayama, Y., Villablanca, J. P., Morino, T., Takahashi, H., Yamauchi, T., Tanishita, K., and Viñuela, F., 2001, "Intraaneurysmal Flow Dynamics Study Featuring an Acrylic Aneurysm Model Manufactured Using a Computerized Tomography Angiogram as a Mold," J. Neurosurg., **95**, pp. 1020–1027.

[16] Tateshima, S., Viñuela, F., Villablanca, J. P., Murayama, Y., Morino, T., Nomura, K., and Tanishita, K., 2003, "Three-Dimensional Blood Flow Analysis in a Wide Necked Internal Carotid Artery-Ophthalmic Artery Aneurysm," J. Neurosurg., **99**, pp. 526–533.

[17] Tateshima, S., Murayama, Y., Villablanca, J. P., Morino, T., Nombra, K., Tanishita, K., and Viñuela, F., 2003, "*In vitro* Measurements of Fluid-Induced Wall Shear Stress in Unruptured Cerebral Aneurysms Harboring Blebs," Stroke, **34**, pp. 187–192.

[18] Ujiie, H., Tachibana, H., Hiramatsu, O., Hazel, A. L., Matsumoto, T., Ogasawara, Y., Nakajima, H., Hori, T., Takakura, K., and Kajiya, F., 1999, "Effects of Size and Shape (aspect ratio) on the Hemodynamics of Saccular Aneurysms: A Possible Index for Surgical Treatment of Intracranial Aneurysms," Neurosurgery, **45**, pp. 119–130.

[19] Jou, L.-D., Saloner, D., and Higashida, R., 2004, "Determining Intra-Aneurysmal Flow for Coiled Cerebral Aneurysms with Digital Fluoroscopy," Biomed. Eng. Appl. Basis Commun., **16**, pp. 43–48.

[20] Jou, L.-D., Quick, C. M., Young, W. L., Lawton, M. T., Higashida, R., Martin, A., and Saloner, D., 2003, "Computational Approach to Quantifying Hemodynamic Forces in Giant Cerebral Aneurysms," AJNR Am. J. Neuroradiol., **24**, pp. 1804–1810.

[21] Foutrakis, G., Yonas, H., and Sclabassi, R., 1999, "Saccular Aneurysm Formation in Curved and Bifurcating Arteries," AJNR Am. J. Neuroradiol., **20**, pp. 1309–1317.

[22] Steinman, D. A., Milner, J. S., Norley, C. J., Lownie, S. P., and Holdsworth, D. W., 2003, "Image-Based Computational Simulation of Flow Dynamics in a Giant Intracranial Aneurysm," AJNR Am. J. Neuroradiol., **24**, pp. 559–566.

[23] Cebral, J. R., Hernández, M., and Frangi, A. F., 2003, "Computational Analysis of Blood Flow Dynamics in Cerebral Aneurysms From CTA and 3D Rotational Angiography Image Data," *International Congress on Computational Bioengineering*, Zaragoza, Spain, Sept. 24–26.

[24] Melbin, P. C. P., and Nesto, R. W., 2002, "Scholarly Review of Geometry and Compliance: Biomechanical Perspectives on Vascular Injury and Healing," ASAIO J., **48**, pp. 337–345.

[25] MacDonald, D. J., Finlay, H. M., and Canham, P. B., 2000, "Directional Wall Strength in Saccular Brain Aneurysms From Polarized Light Microscopy," Ann. Biomed. Eng., **28**, pp. 533–542.

[26] Hsiai, T. K., Cho, S. K., Honda, H. M., Hama, S., Navab, M., Demer, L. L., and Ho, C. M., 2002, "Endothelial Cell Dynamics Under Pulsating Flows: Significance of High Versus Low Shear Stress Slew Rates ($\partial \tau / \partial t$)," Ann. Biomed. Eng., **30**, pp. 646–656.

[27] Zhao, S. Z., Xu, X. Y., Hughes, A. D., Thom, S. A., Stanton, A. V., Ariff, B., and Long, Q., 2000, "Blood Flow and Vessel Mechanics in a Physiologically Realistic Model of a Human Carotid Arterial Bifurcation," J. Biomech., **33**, pp. 975–984.

[28] Gijsen, F. J. H., van de Vosse, F. N., and Janssen, J. D., 1999, "The Influence of the Non-Newtonian Properties of Blood on the Flow in Large Arteries: Steady Flow in a Carotid Bifurcation Model," J. Biomech., **32**, pp. 601–608.

[29] Ma, B., Harbaugh, R. E., and Raghavan, M. L., 2004, "Three-Dimensional Geometrical Characterization of Cerebral Aneurysms," Ann. Biomed. Eng., **32**, pp. 264–273.

[30] Raghavan, M. L., Ma, B., and Harbaugh, R. E., 2005, "Quantified Aneurysm Shape and Rupture Risk," J. Neurosurg., **102**, pp. 355–362.

[31] Parlea, L., Fahrig, R., Holdsworth, D. W., and Lownie, S. P., 1999, "An Analysis of the Geometry of Saccular Intracranial Aneurysms," AJNR Am. J. Neuroradiol., **20**, pp. 1079–1089.

[32] Johnston, B. M., Johnston, P. R., Corney, S., and Kilpatrick, D., 2004, "Non-Newtonian Blood Flow in Human Right Coronary Arteries: Steady State Simulations," J. Biomech., **37**, pp. 709–720.

[33] Kim, S., 2002, *A study of non-Newtonian viscosity and yield stress of blood in a scanning capillary-tube rheometer*, thesis, Drexel University, Philadelphia, PA.

[34] Guppy, K. H., Charbel, F. T., Corsten, L. A., Zhao, M., and Debrum, G., 2002, "Hemodynamic Evaluation of Basilar and Vertebral Artery Angioplasty," Neurosurgery, **51**, pp. 327–333.

[35] Owega, A., Klingelhöfer, J., Sabri, O., Jürgen, H., Albers, M., Saß, H., 1998, "Cerebral Blood Flow Velocity in Acute Schizophrenic Patients: A Transcranial Doppler Ultrasonography Study," Stroke, **29**, pp. 1149–1154.

[36] Holdsworth, D. W., Norley, C. J. D., Frayne, R., Steinmam, D. A., and Rutt, B. K., 1999, "Characterization of Common Carotid Artery Blood-Flow Waveforms in Normal Human Subjects," Physiol. Meas, **20**, pp. 219–240.

[37] Schweizer, J., Mück-Weymann, M., and Klemm, E., 1996, "Messung des Basilaris-flußgeschwindigkeit Mittels TCD und TCCD," Ultraschall Med., **17**, pp. 68–71.

[38] Baumgartner, R. W., Schmid, C., and Baumgartner, I., 1996, "Comparative Study of Power-Based Versus Mean Frequency-Based Transcranial Color-Codex Duplex Sonography in Normal Adults," Stroke, **27**, pp. 101–104.

[39] Zamir, M., 2000, *The physics of pulsatile flow*, Springer-Verlag, New York.

[40] Ferziger, J. H., Perić, M., 1997, *Computational methods for fluid dynamics*, Springer-Verlag, Berlin.

[41] Cebral, J. R., Castro, M. A., Appanaboyina, S., Putman, Ch. M., Millan, D., Frangi, A. F., 2005, "Efficient Pipeline for Image-Based Patient-Specific Analysis of Cerebral Aneurysm Hemodynamics: Technique and Sensitivity," IEEE Trans. Med. Imaging, **24**, pp. 457–467.

[42] Shojima, M., Oshima, M., Takagi, K., Torii, R., Hayakawa, M., Katada, K., Morita, A., and Kirino, T., 2004, "Magnitude and Role of Wall Shear Stress on Cerebral Aneurysm Computational Fluid Dynamic Study of 20 Middle Cerebral Artery Aneurysms," Stroke, **35**, pp. 2500–2505.

[43] Hoi, Y., Meng, H., Woodward, S. H., Bendok, B. R., Hanel, R. A., Guterman, L. R., and Hopkins, L. N., 2004, "Effects of Arterial Geometry on Aneurysm Growth: Three-Dimensional Computational Fluid Dynamics Study," J. Neurosurg., **101**, pp. 676–681.

[44] Steinman, D. A., Kehoe, S. C., Ford, M. D., Nikolov, H. N., and Holdsworth, D. W., 2003, "Dancing on the Knife-Edge of Symmetry: On the Misuse of Symmetric Models for Studying Blood Flow Dynamics," *Proceedings of ASME 2003 Summer Bioengineering Conference*, Key Biscayne, FL, June 25–29, pp. 1251–1252.

[45] Hassan, T., Timofeev, E. V., Saito, T., Shimizu, H., Ezura, M., Tominaga, T., Takahashi, A., and Takayama, K., 2004, "Computational Replicas: Anatomic Reconstructions of Cerebral Vessels as Volume Numerical Grids at Three-Dimensional Angiography," AJNR Am. J. Neuroradiol., **25**, pp. 1356–1365.